Fermi surface and carrier compensation of pyrite-type $PtBi_2$ revealed by quantum oscillations

Lingxiao Zhao, Liangcai Xu, Huakun Zuo, Xuming Wu, Guoying Gao, and Zengwei Zhu*

Wuhan National High Magnetic Field Center School of Physics, Huazhong University of Science and Technology, Wuhan 430074, China

(Received 22 April 2018; published 23 August 2018)

Large nonsaturating magnetoresistance has been observed in various materials and electron-hole compensation has been regarded as one of the main mechanisms. Here we present a detailed study of the angle-dependent Shubnikov–de Haas effect on large magnetoresistance material pyrite-type $PtBi_2$, which allows us to experimentally reconstruct its Fermi-surface structure and extract the physical properties of each pocket. We find its Fermi surface contains four types of pockets in the Brillouin zone: three ellipsoidlike hole pockets α with C_4 symmetry located on the edges (M points), one intricate electron pocket β merged from four ellipsoids along [111] located on the corners (R points), and two smooth and cambered octahedrons γ (electron) and δ (hole) on the center (Γ point). The deduced carrier densities of electrons and holes from the volume of pockets prove carrier compensation. This compensation at low temperatures is also supported by fitting the field dependence of Hall and magnetoresistance at different temperatures. We conclude that the compensation is the main mechanism for the large nonsaturating magnetoresistance in pyrite-type $PtBi_2$. We found the hole pockets α may contribute major mobility because of their light masses and anisotropy to relatively avoid large-angle scattering at low temperature. This may be a common feature of semimetals with large magnetoresistance. The found subquadratic magnetoresistance in high field is probably due to field-dependent mobilities, another feature of semimetals under high magnetic fields.

DOI: 10.1103/PhysRevB.98.085137

I. INTRODUCTION

Large magnetoresistance and its mechanisms [1–5] have drawn tremendous new interest beginning with the discovery of WTe_2 [6]. Following this discovery, nonmagnetic materials such as Cd_3As_2 [7], WP_2 [8], LaSb [9], $TaAs_2$ [10], YSb [11], NbP [12], α-As [13], $NbSb_2$ [14], and more recently pyrite-type $PtBi_2$ [15] have been discovered to show large magnetoresistance. In contrast to the "conventional" semimetals, bismuth [16] and graphite [17], these materials show nonsaturating magnetoresistance as high magnetic field is increased. Several mechanisms have been proposed to explain it. The first mechanism is the electron-hole compensation scenario which has been ascribed to most of the cases listed above, and also other materials [6,8,18–20]. Under the e-h "resonance" condition ($n_e = n_h$), the magnetoresistivity $\rho(B) \simeq \frac{B^2}{ne}\frac{\mu_e\mu_h}{\mu_e+\mu_h}$ never saturates and exhibits a quadratic dependence in magnetic field, where n_e (n_h) and μ_e (μ_h) are the density and mobility of electrons (holes). Other mechanisms range from topological protection [7,9,21] to metal-insulator transition by magnetic field [22,23].

Recently, pyrite-type $PtBi_2$ was predicated a three-dimensional Dirac semimetal [24]. Following the prediction, large nonsaturating magnetoresistance has been experimentally observed in pyrite-type $PtBi_2$ [15] and its magnetoresistance is in the front rank of the discovered materials, reaching $1.12\times10^7\%$ at 1.8 K and 33 T. The origin of the large magnetoresistance was preliminarily discussed based on the compensation scenario by fitting with a two-band model [15]. But the detailed Fermi surface and its relation to large magnetoresistance are missing in the previous study [15]. On the other hand, maybe due to the difficulty of peeling the pyrite-structure sample, angle-resolved photoemission spectroscopy (ARPES) data also have not been reported yet. Unlike its hexagonal polymorph $PtBi_2$, ARPES results [25,26] suggest a Dirac-cone-like dispersion may lead to its unconventional large linear magnetoresistance [27,28].

In this paper, we reveal that the compensation of $PtBi_2$ would be the mechanism for the large nonsaturating magnetoresistance by verifying the e-h balance through mapping of the Fermi surface directly by the angle dependence of the Shubnikov–de Haas effect (SdH) and also by a two-band model from the temperature dependence of Hall resistivity and magnetoresistivity. Our mapped Fermi surface from the angle dependence of the SdH suggests four types of Fermi pockets instead of three types of pockets from the previous calculation [15]: three equivalent hole ellipsoidlike pockets named α on the edge (M of the Brillouin zone), one electron pocket named β located on the corners (R), and a small octahedronlike electron pocket (γ) and a large octahedron hole pocket (δ) at the center (Γ) of the Brillouin zone. The electron-hole ratio is compensated within an accuracy of 1% after summing up the carrier densities from whole obtained pockets by their types. This compensation is also supported by our two-band fitting for the temperature dependence of Hall and magnetoresistance.

II. EXPERIMENT

Pyrite-type $PtBi_2$ single crystals were grown by the flux method with a Pt:Bi = 1:20 molar ratio. Pt powder (99.95%) and Bi grains (99.999%) were mixed and sealed in an evacuated

*zengwei.zhu@hust.edu.cn

quartz ampoule. The ampoule was heated to 450 °C and preserved for 10 h, then cooled down to 300 °C in 150 h. After centrifugalizing, single crystals were separated from the flux. The dimension of a typical as-grown sample is around $2\times2\times2$ mm^3. The sample was then cut into a narrow strip by a wire saw to carry on transport measurement. The measurement was performed in a TeslatronPT (Oxford Instruments) equipped with a homemade rotator whose angle can be controlled by a data-collecting computer. Angles of the motor-driven rotator were determined either by a Hall probe on the sample holder or by steps from the driving motor which was calibrated before measurement. The two angle-determining methods show good consistency. The electrical current was applied by a Keithley 6221 and the voltage was measured by a Keithley 2182A. The magnetic field was perpendicular to the current during rotation. The high-magnetic-field magnetoresistance measurement was performed at the Wuhan National High Magnetic Field Center. A 100 kHz ac current was applied by a NI-5402 signal generator and voltage was recorded by a NI-5105 high-speed digitizer which worked in 4 MHz. A digital phase lock-in method was applied to extract magnetoresistance.

III. RESULTS AND DISCUSSION

Figure 1 shows the temperature dependence of resistivity $\rho_0(T)$ of the measured sample which has a residual resistivity ratio RRR $= \rho(300\text{ K})/\rho(1.7\text{ K})$ of 546. More samples with different RRR were measured and show the same quantum-oscillation results. Both resistivities at room temperature of 132 and 0.24 $\mu\Omega$ cm at 1.7 K are higher than those reported [15]. Such differences may be due to the different sample quality or the different orientations of the applied current. Note that the current was injected along [0$\bar{1}$1] in the previous report [15] while it was along [100] in our case, which could induce a difference in carrier mobility. For instance, the mobility is closely related to the orientation of the applied current in bismuth [29]. The inset of Fig. 1 shows the x-ray diffraction pattern of the photographed sample whose crystallographic direction [010] is labeled with a blue arrow. The sharpness of the (002) indicates the high quality of the sample.

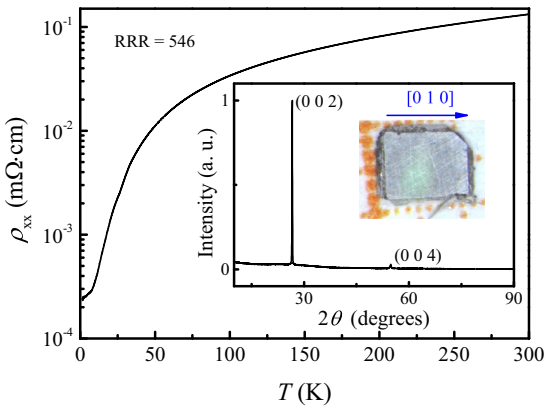

FIG. 1. Temperature dependence of resistivity from 1.7–300 K. The residual resistivity ratio $\rho(300\text{ K})/\rho(1.7\text{ K})$ is about 546. The inset shows the x-ray diffraction pattern of the (001) facet of the photographed sample which was then cut into a smaller sample for measurements. The current was along the [010] orientation during whole measurements.

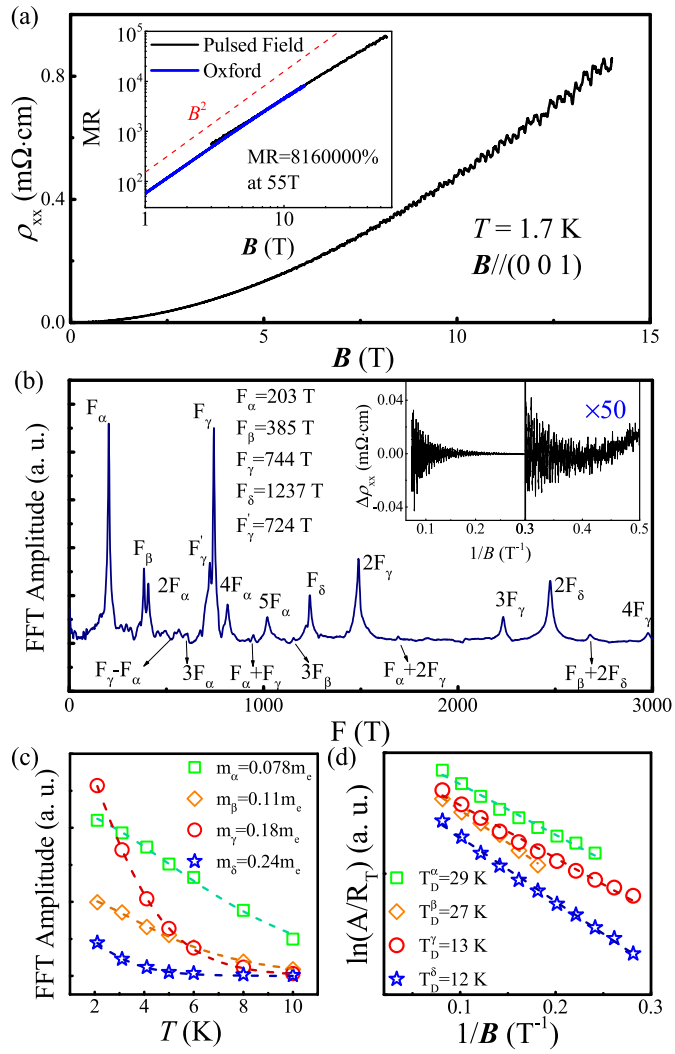

FIG. 2. (a) Field-dependent $\rho(B)$ curve at 1.7 K as magnetic field along [001] and the current along [100] using a TeslatronPT from Oxford Instruments. The inset shows the MR ($[\rho(B)-\rho(0)]/\rho(0)\times100\%$) from the same data in the blue curve and also with data from pulsed fields up to 55 T where the MR reaches 8 160 000%. The MR curve has a subquadratic dependence in magnetic fields while a red-dashed B^2 curve is offset for comparison. (b) FFT spectra of SdH oscillations after subtracting the background from magnetoresistance. The SdH oscillations as a function of $1/B$ are also shown in the inset. The oscillations start at as low as 2 T indicating high mobility of the sample. We also indexed the sharp peaks of the FFT spectra accordingly. (c),(d) The cyclotron masses and Dingle temperatures of different pockets as field along [001] extracted from the temperature dependence of the SdH effect with the Lifshitz-Kosevich theorem [30].

Figure 2(a) displays a typical field-dependent $\rho(B)$ curve with pronounced SdH oscillations at 1.7 K with the magnetic field along [001] and the current along [100]. The inset shows the magnetoresistance (MR) ($[\rho(B)-\rho(0)]/\rho(0)\times100\%$) ~817 300% at 14 T from the same data and also shows MR up to ~8 160 000% at 55 T without any signature of saturation

measured in a pulsed magnet. These results confirm the large nonsaturating magnetoresistance in pyrite-type $PtBi_2$; even the RRR is lower than that reported in [15]. The MR curve can be fitted with a power law $MR = aB^{1.79\pm0.02}$, deviating from a quadratic dependence in field. The inset of Fig. 2(b) presents the SdH oscillations after subtracting the background by a polynomial fitting. The SdH oscillations can be clearly seen from $B = 2$ T, indicating high carrier mobility of the sample by a first approximation to have the mobility of $\mu \geqslant 0.5\ \mathrm{T}^{-1}$. These oscillations allow us to extract the fine structure of the Fermi surface. The SdH oscillations as a function of $1/B$ are also shown in the inset; these oscillations are observable down to $0.5\ \mathrm{T}^{-1}$ after enlarging 50 times. We then obtain fast Fourier transform (FFT) spectra of SdH oscillations and plot them in Fig. 2(b). Each FFT peak at the fundamental or higher harmonics can calibrate the extremal Fermi surface area which is perpendicular to the magnetic field [30]. We can clearly identify and index the sharp peaks of the FFT spectra for four different frequencies named α, β, γ, and δ in Fig. 2(b). Note that the amplitude of the second-harmonic frequency of δ is higher than that of the fundamental frequency. This is probably due to spin splitting of this band [30] and is confirmed in our later angle dependence of the SdH effect: the amplitude of the fundamental frequency of δ becomes larger as a normal oscillation series does after the rotation. The small amplitude of $3F_\alpha$ is also due to spin splitting [31]. The cyclotron masses and Dingle temperatures for four pockets as field along [001] are shown in Figs. 2(c) and 2(d), extracted from the SdH curves at different temperatures with the Lifshitz-Kosevich formula [30] by the attenuation factors due to finite temperature: $R_T = \frac{X}{\sinh X}$ and impurity scattering $R_D = \exp(-\frac{\pi m^*}{eB\tau_D})$ where $X = \frac{2\pi^2 k_B T m^*}{e\hbar B}$. We note that our results are not exactly the same as those in Ref. [15], where a different orientation of magnetic field is applied along [111]. We tried the de Haas–van Alphen (dHvA) effect and find similar masses from the SdH [31] in our case. We also notice that the theoretical results proposed three pockets in Ref. [15], instead of the four pockets found in the current work. Fine-tuning of the parameters is probably needed for the theoretical calculation since the spin-orbit coupling and electron correction should play important roles in the compound.

Now we can map the Fermi surface by rotating the sample to get the angle dependence of SdH; the schematic diagram of the sample geometry is shown in Fig. 3(a). Through the above procedure, we obtained the FFT spectra of SdH at various angles by rotating the sample at 1.7 K from [001] to [00$\bar{1}$]. Figure 3(b) shows the shifted FFT spectra every 5° from 0 [001] to 90° [010]. We have not shown the data beyond 90°, since the angle dependence of the SdH pattern exactly repeats because of its cubic crystal structure nature. Figure 3(c) shows the angle dependence of the FFT peaks in different symbols. The branch $F_{\alpha_1}(\theta)$ displaces 90° from the branch $F_{\alpha_2}(\theta)$. So we deduce that the three equivalent α pockets locate on the edge because of their C_4 symmetry with an assumption that pockets always have the highest symmetric locations. This assumption is also for determining locations of other types of pockets. Another almost constant frequency $F_{\alpha_3}(\theta)$ spectrum is absent in the current results. This absence should be due to the lower mobility when the current is along the long axis of the α_3 ellipsoid, as seen in YSb [11]. Then for the α pockets which are prolate spheroids, we fitted the angle dependence of F_{α_1} quantitatively by the following equation:

$$F_{\alpha_i} = F_0/\sqrt{(\cos[\theta-(i\text{–}1)\pi/2])^2+(\lambda\ \sin[\theta-(i\text{–}1)\pi/2])^2}, \tag{1}$$

where we can obtain $F_0 = 202$ T, $\lambda = 0.55$ and "i" is for the subscript of α. By Onsager relation $F = (\hbar/2\pi e)A_k$ between frequency F and the extreme cross section A_k of a Fermi surface, we extracted the values listed in Table I. The carrier density for each equivalent α prolate spheroid is $0.29\times10^{20}\ \mathrm{cm}^{-3}$. The type of this pocket is hole, by using the previous calculations [15] as a guide. The types of other pockets are deduced by the same route.

The β pocket has quite a complicated structure, but can be sorted out. We first exclude that these ellipsoids exist independently, locating between Γ and R along [111]. The shape

TABLE I. Summary of physical properties: volume, quantity, carrier density (n), cyclotron mass (m_{cyc}), dingle temperature T_D, relaxation time τ_D, and mobility (μ_D) of α, β, γ, and δ pockets. The momentum (k_a, k_b, and k_c), k_{edge}, and k_s were axes of an ellipsoid, an edge length of the octahedron Fermi surface, and a radius of the sphere in the middle of β, respectively.

	α (h)	β (e)	γ (e)	δ (h)
Location	Edge (M)	Corner (R)	Center (Γ)	Center (Γ)
k (Å^{-1})		Mid. sphere		
		$k_s = 0.1094$		
	$k_a = 0.0777$	Ellipsoids	$k_{\mathrm{edge}} = 0.198$	$k_{\mathrm{edge}} = 0.257$
	$k_b = 0.0777$	$k_a = 0.0792$		
	$k_c = 0.143$	$k_b = 0.0792$		
		$k_c = 0.1584$		
V (Å^{-3})	0.0036	0.0221	0.0104	0.0225
Number	3	1	1	1
n (cm^{-3})	0.87×10^{20}	1.88×10^{20}	0.84×10^{20}	1.82×10^{20}
Fraction	1.32%	2.68%	1.26%	2.73%
m_{cyc} (m_e)	0.078 ± 0.001	0.11 ± 0.01	0.18 ± 0.01	0.24 ± 0.01
T_D (K)	29	27	13	12
τ_D (s)	4.2×10^{-14}	4.5×10^{-14}	9×10^{-14}	1×10^{-13}
μ_D (cm^2/V s)	944	719	913	742

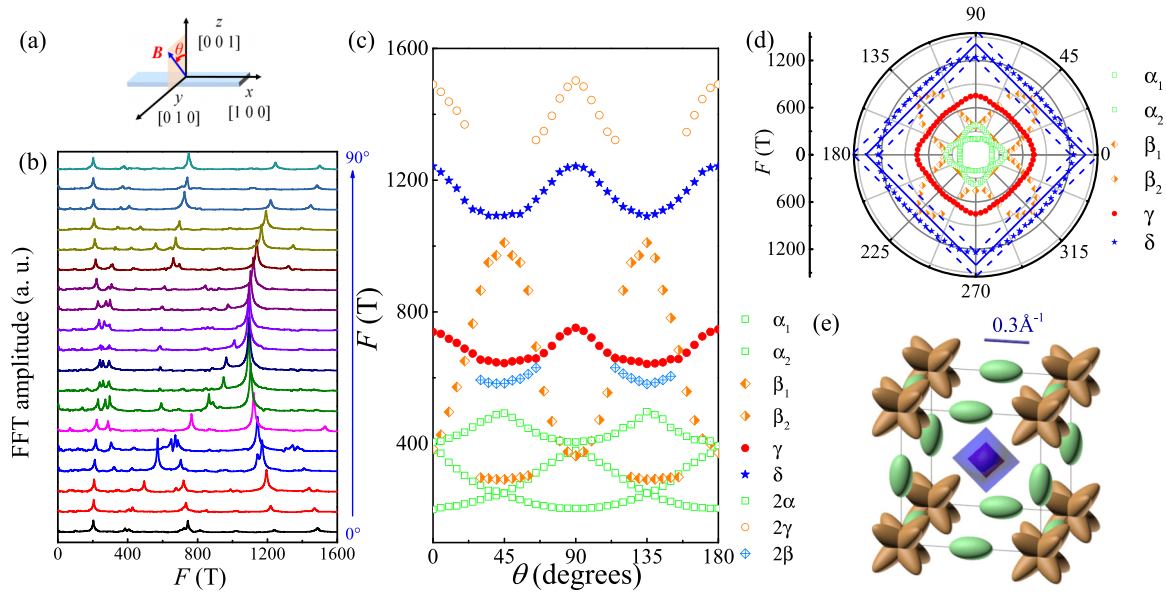

FIG. 3. (a) Schematic diagram of the sample geometry for measurement. The magnetic field was rotated in the [001]-[010] plane as the current along [100]. (b) Shifted FFT spectra of SdH as a function of frequency every 5° from 0 to 90°. (c) Angular dependence of SdH frequencies. The symbols are for experimental data from the peaks of the FFT spectra. We can identify four fundamental frequencies and their harmonic frequencies. (d) The fundamental frequencies of four pockets in a polar plot where two octahedronlike Fermi pockets (δ and γ) can be easily identified, besides ellipsoidlike pockets α and β. In the fitting of the octahedron, we take the geometric mean (in the solid line) of two minimal and maximal edge lengths shown in dashed lines for the length of its edge. (e) Fermi-surface reconstruction from the fitted parameters. The locations of pockets are determined from symmetric and size arguments (see the main text). A scale bar is also shown.

from $F_\beta(\theta)$ resembles that of an ellipsoid, but is rotated 45° along the [100] axis at first glimpse. According to the highest symmetry requirement, the long axis of the ellipsoid should lie at [111] to have a maximum cross section of an ellipsoid at 45° in the current case. Note that this ellipsoid is then tilted when the field is rotated, as the rotating axis is not along its major or minor axis. Then Eq. (1) is no longer valid for this case. By geometric consideration of an independent ellipsoid, we obtain its semiminor axis $k_a = k_b = 0.094$ Å^{-1} and its semimajor axis $k_c = 0.33$ Å^{-1} from the FFT values at high symmetric angles. But the β band will touch two other bands γ and δ (discussed below) by considering that two semimajor axes of β bands lie along [111] according to the symmetry, note that the diagonal length of the Brillouin zone is 1.62 Å^{-1}. More quantum oscillations are expected from this touching, which contradicts our observations. Besides, the carrier density from eight such pockets would surpass 10^{21} cm^{-3}, which contrasts with the semimetal property from its resistivity. Therefore, these β pockets should depend on and have to cross each other, leading to a reduction of the total number of ellipsoids and also their length [illustrated in Fig. 3(d)]. We obtain the volume of this pocket through summing up the volume of four ellipsoids whose middle parts are truncated and one middle sphere. By considering the frequencies of an ellipsoid tilted along [111] when the field is at 0, 45° and also the fact that the electrons actually travel across two connected ellipsoids at $\theta = 0$ in this case, we extract actual $k_a = k_b = 0.0792$ Å^{-1} and $k_c = 0.1584$ Å^{-1} and the radius of the middle sphere is $k_s = 0.1094$ Å^{-1} from the lower frequency of F_β at 45°. Finally, the carrier density of 1.88×10^{20} cm^{-3} for this electronlike pocket is obtained.

Although the shape is not an exact square in the polar plot Fig. 3(d) as for an octahedron, we can still treat the γ and δ bands as two smooth and cambered octahedrons whose symmetry naturally meet the requirement of a cubic. This cambered surface induces a warping effect to have additional F'_γ which have the same angle-dependent behavior as F_γ [31], but vanishes at larger angles. These octahedrons should locate at the corner or the middle of the Brillouin zone because of their high symmetry. Under this assumption, we calculated the geometric mean of the edge length [the solid line in Fig. 3(d)] of the minimal and maximal octahedron of δ which are able to encircle the band [the dashed lines in Fig. 3(d)]. The same procedure is used to obtain the edge length of the octahedron for γ. After calculating volumes, we deduce that the densities of the electronlike γ and the holelike δ are 0.84×10^{20} and 1.82×10^{20} cm^{-3}, respectively.

Figure 3(e) is a scale drawing in a certain scale (a scale bar is shown), in which we summarized and reconstructed the Fermi surface according to our SdH results. Note that the symmetries of β, γ, and δ are the same. So another possibility for locations of pockets is that γ and δ locate on the corners and β is at the center of the Brillouin zone. However, the total hole (α and δ) and electron (β and γ) carrier densities not affected in the two cases are 2.69×10^{20} and 2.73×10^{20}cm^{-3}, respectively. This result suggests compensation between electrons and holes at a ratio of 0.99. The carrier densities are typical for semimetals, such as $WTe_2(6.6\times10^{19})$ [18], $LaSb(1.1\times10^{20})$ [9], $Sb(5.5\times10^{19})$ [32], $WP_2(1.4\times10^{20})$ [8], and also α-$As(1.1\times10^{20})$ [13]. And all their mobilities are around 10^5 (up to 10^6 in Sb) cm^2 V^{-1} s^{-1}. Such shared common properties may be the key to understanding large magnetoresistance [33]. For a compensated semimetal, we would expect a quadratic

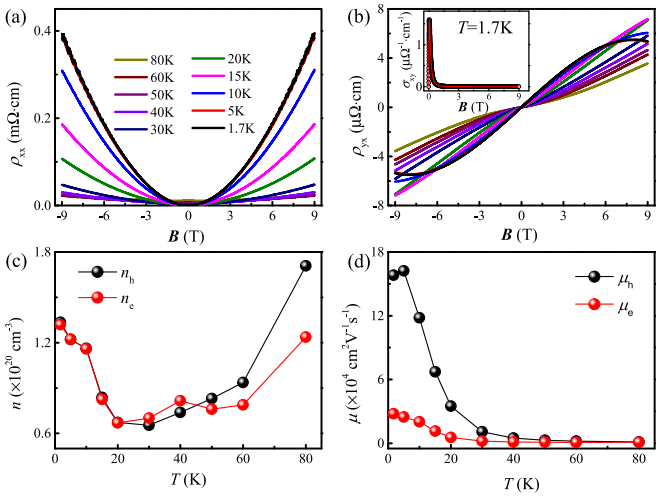

FIG. 4. (a) Temperature dependence of magnetoresistance and (b) Hall resistivity in different temperatures. The inset shows a red fitting line from the two-band model and black σ_{xy} symbols measured at 1.7 K. (c), (d) Temperature dependence of carrier densities $n_{e,h}$ and $\mu_{e,h}$. The two-band model again supports the compensation of electron and hole from the Fermi-surface method.

dependence of magnetoresistance, but the MR $= aB^{1.79\pm0.02}$ in this material. Such deviation of the quadratic dependence of magnetoresistance is prevalent, due to an unavoidable field-induced reduction in mobility by disorders [34].

To further illustrate the compensation, we carried out temperature dependence of magnetoresistance and Hall resistivity, shown in Figs. 4(a) and 4(b), and found a similar result as in the previous report [15]. We extracted the carrier densities and mobilities by fitting the Hall conductivity by the two-band model [13,35,36]:

$$\sigma_{xy}(B) = \frac{\rho_{yx}(B)}{\rho_{xx}^2(B) + \rho_{yx}^2(B)} = \left[\frac{n_h\mu_h^2}{1+(\mu_h B)^2} - \frac{n_e\mu_e^2}{1+(\mu_e B)^2}\right]eB,$$

present in Figs. 4(c) and 4(d). Although there is a slight discrepancy between electron and holes at the high-temperature range, the carrier density between two types of carriers becomes equal below 20 K and the ratio n_e/n_h is about 0.99 at 1.7 K from fitting. The carrier densities $n_e = 1.32\times10^{20}$ cm^{-3} and $n_h = 1.33\times10^{20}$ cm^{-3} are also quite close to the values from the Fermi-surface method. This two-band model gives relatively lower numbers which should be higher since the carrier density easily surpasses 1.8×10^{20} cm^{-3} even only from the δ band. Two other two-band fitting methods from magnetoconductivity and Hall resistivity shown in the Supplemental Material [31] again exhibit compensation of carriers, but get higher carrier densities. The difference of carrier densities between different fitting methods indicates the limitation of two-band fitting for a multiband system.

The mobility of holes increases faster than that of electrons to 1.5×10^5 cm^2/V s as the temperature is lowered. This increase of hole mobility may mainly result from the contribution of α pockets which have the lightest masses and their anisotropy ($k_c/k_a \simeq 2$). Such two features are prevalent in the semimetals at least in one of their Fermi pockets: Sb [32,34] ($m^* \sim 0.088m_e$, anisotropy of $k \sim 5.2$), bismuth [37] ($m^* \sim 0.0011m_e$, anisotropy of $k \sim 15$), YSb [11,36,38] ($m^* \sim 0.2m_e$, anisotropy of $k \sim 2$), and WTe_2 [18,39] ($m^* \sim 0.4m_e$, anisotropy of $k \sim 2$–3). The $\frac{\mu_T}{\mu_D}$ is around 150 and 25 for holes and electrons, respectively, and μ_T is the mobility from the two-band fitting. This indicates that a small-angle-scattering process in quantum oscillation plays a significant role during carrier transport after electron-phonon scattering has faded as the temperature is decreased, which may be a common feature in semimetals [34]. The quantum oscillation mobilities are integral to all the scattering angles, while the mobilities of Hall effect are only affected by large-angle scattering [15,34]. So, to have a pocket with light mass and anisotropy may relatively avoid large-angle scattering at low temperature to have higher transport mobility.

IV. CONCLUSION

In summary, we have experimentally mapped out the Fermi surface of pyrite-type $PtBi_2$ including two hole and two electron pockets by angle dependence of SdH measurements. This allows us to deduce the carrier density and mobility of each pocket and to reveal a compensation between the electron and hole. Such compensation is further supported by two-band fitting from the temperature dependence of magnetoresistance and Hall resistivity. We ascribed the large nonsaturating magnetoresistance found in this material to the compensation. The high hole mobility may be due to the light mass and anisotropy of α pockets.

ACKNOWLEDGMENTS

We acknowledge useful discussions with Kamran Behnia, Benoît Fauqué, and Gang Xu. We acknowledge our engineering team in the WHMFC for realizing the 80 T measurement. This work is supported by the 1000 Youth Talents Plan, the National Science Foundation of China (Grants No. 11574097 and No. 51861135104), the National Key Research and Development Program of China (Grant No. 2016YFA0401704), and the China Postdoctoral Science Foundation (2018M630846).

[1] J. H. Mangez, J. P. Issi, and J. Heremans, Phys. Rev. B **14**, 4381 (1976).
[2] G. B. Yntema, Phys. Rev. **91**, 1388 (1953).
[3] D. E. Soule, Phys. Rev. **112**, 698 (1958).
[4] E. Mun, H. Ko, G. J. Miller, G. D. Samolyuk, S. L. Bud'ko, and P. C. Canfield, Phys. Rev. B **85**, 035135 (2012).
[5] H. Takatsu, J. J. Ishikawa, S. Yonezawa, H. Yoshino, T. Shishidou, T. Oguchi, K. Murata, and Y. Maeno, Phys. Rev. Lett. **111**, 056601 (2013).
[6] M. N. Ali, J. Xiong, S. Flynn, J. Tao, Q. D. Gibson, L. M. Schoop, T. Liang, N. Haldolaarachchige, M. Hirschberger, N. P. Ong, and R. J. Cava, Nature (London) **514**, 205 (2014).

[7] T. Liang, Q. Gibson, M. N. Ali, M. Liu, R. J. Cava, and N. P. Ong, Nat. Mater. **14**, 280 (2015).

[8] N. K. Y. Sun, N. Xu, K. Manna, M. Yao, V. Süss, I. Leermakers, O. Young, T. Förster, M. Schmidt, H. Borrmann, B. Yan, U. Zeitler, M. Shi, C. Felser, and C. Shekhar, Nat. Commun. **8**, 1642 (2017).

[9] F. F. Tafti, Q. D. Gibson, S. K. Kushwaha, N. Haldolaarachchige, and R. J. Cava, Nat. Phys. **12**, 272 (2015).

[10] Y.-Y. Wang, Q.-H. Yu, P.-J. Guo, K. Liu, and T.-L. Xia, Phys. Rev. B **94**, 041103 (2016).

[11] J. Xu, N. J. Ghimire, J. S. Jiang, Z. L. Xiao, A. S. Botana, Y. L. Wang, Y. Hao, J. E. Pearson, and W. K. Kwok, Phys. Rev. B **96**, 075159 (2017).

[12] C. Shekhar, A. K. Nayak, Y. Sun, M. Schmidt, M. Nicklas, I. Leermakers, U. Zeitler, Y. Skourski, J. Wosnitza, Z. Liu, Y. Chen, W. Schnelle, H. Borrmann, Y. Grin, C. Felser, and B. Yan, Nat. Phys. **11**, 645 (2015).

[13] L. Zhao, Q. Xu, X. Wang, J. He, J. Li, H. Yang, Y. Long, D. Chen, H. Liang, C. Li, M. Xue, J. Li, Z. Ren, L. Lu, H. Weng, Z. Fang, X. Dai, and G. Chen, Phys. Rev. B **95**, 115119 (2017).

[14] K. Wang, D. Graf, L. Li, L. Wang, and C. Petrovic, Sci. Rep. **4**, 7328 (2014)

[15] W. Gao, N. Hao, F.-W. Zheng, W. Ning, M. Wu, X. Zhu, G. Zheng, J. Zhang, J. Lu, H. Zhang, C. Xi, J. Yang, H. Du, P. Zhang, Y. Zhang, and M. Tian, Phys. Rev. Lett. **118**, 256601 (2017).

[16] B. Fauqué, B. Vignolle, C. Proust, J.-P. Issi, and K. Behnia, New J. Phys. **11**, 113012 (2009).

[17] B. Fauqué and K. Behnia, in *Basic Physics of Functionalized Graphite*, edited by P. D. Esquinazi (Springer, New York, 2016), Chap. 4.

[18] Z. Zhu, X. Lin, J. Liu, B. Fauqué, Q. Tao, C. L. Yang, Y. G. Shi, and K. Behnia, Phys. Rev. Lett. **114**, 176601 (2015).

[19] L.-K. Zeng, R. Lou, D.-S. Wu, Q. N. Xu, P.-J. Guo, L.-Y. Kong, Y.-G. Zhong, J.-Z. Ma, B.-B. Fu, P. Richard, P. Wang, G. T. Liu, L. Lu, Y.-B. Huang, C. Fang, S.-S. Sun, Q. Wang, L. Wang, Y.-G. Shi, H. M. Weng, H.-C. Lei, K. Liu, S.-C. Wang, T. Qian, J.-L. Luo, and H. Ding, Phys. Rev. Lett. **117**, 127204 (2016).

[20] P.-J. Guo, H.-C. Yang, B.-J. Zhang, K. Liu, and Z.-Y. Lu, Phys. Rev. B **93**, 235142 (2016).

[21] X. H. Niu, D. F. Xu, Y. H. Bai, Q. Song, X. P. Shen, B. P. Xie, Z. Sun, Y. B. Huang, D. C. Peets, and D. L. Feng, Phys. Rev. B **94**, 165163 (2016).

[22] D. V. Khveshchenko, Phys. Rev. Lett. **87**, 206401 (2001).

[23] Y. Kopelevich, J. C. Medina Pantoja, R. R. da Silva, and S. Moehlecke, Phys. Rev. B **73**, 165128 (2006).

[24] Q. D. Gibson, L. M. Schoop, L. Muechler, L. S. Xie, M. Hirschberger, N. P. Ong, R. Car, and R. J. Cava, Phys. Rev. B **91**, 205128 (2015).

[25] S. Thirupathaiah, Y. Kushnirenko, E. Haubold, A. V. Fedorov, E. D. L. Rienks, T. K. Kim, A. N. Yaresko, C. G. F. Blum, S. Aswartham, B. Büchner, and S. V. Borisenko, Phys. Rev. B **97**, 035133 (2018).

[26] Q. Yao, Y. P. Du, X. J. Yang, Y. Zheng, D. F. Xu, X. H. Niu, X. P. Shen, H. F. Yang, P. Dudin, T. K. Kim, M. Hoesch, I. Vobornik, Z.-A. Xu, X. G. Wan, D. L. Feng, and D. W. Shen, Phys. Rev. B **94**, 235140 (2016).

[27] C. Q. Xu, X. Z. Xing, X. F. Xu, B. Li, B. Chen, L. Q. Che, X. Lu, J. H. Dai, and Z. X. Shi, Phys. Rev. B **94**, 165119 (2016).

[28] X. Yang, H. Bai, Z. Wang, Y. Li, Q. Chen, J. Chen, Y. Li, C. Feng, Y. Zheng, and Z.-a. Xu, Appl. Phys. Lett. **108**, 252401 (2016).

[29] A. Collaudin, B. Fauqué, Y. Fuseya, W. Kang, and K. Behnia, Phys. Rev. X **5**, 021022 (2015).

[30] D. Shoenberg, *Magnetic Oscillations in Metals* (Cambridge University Press, Cambridge, UK, 2009).

[31] See Supplemental Material at http://link.aps.org/supplemental/10.1103/PhysRevB.98.085137 for the extraction of effective mass from dHvA, magnetoresistance up to 80 T, the quantum oscillations of Hall resistivity, the amplitude of $3F_{\alpha}$, discussion on F_{γ} and F_{δ} do not come from Zeeman effect of one band and carriers' densities and mobilities fitted by magnetoconductivity and Hall resistivity.

[32] L. R. Windmiller, Phys. Rev. **149**, 472 (1966)

[33] K. Behnia, J. Phys.: Condens. Matter **27**, 375501 (2015)

[34] B. Fauqué, X. Yang, W. Tabis, M. Shen, Z. Zhu, C. Proust, Y. Fuseya, and K. Behnia, arXiv:1803.00931.

[35] J. He, C. Zhang, N. J. Ghimire, T. Liang, C. Jia, J. Jiang, S. Tang, S. Chen, Yu He, S.-K. Mo, C. C. Hwang, M. Hashimoto, D. H. Lu, B. Moritz, T. P. Devereaux, Y. L. Chen, J. F. Mitchell, and Z.-X. Shen, Phys. Rev. Lett. **117**, 267201 (2016)

[36] O. Pavlosiuk, P. Swatek, and P. Wiśniewski, Sci. Rep. **6**, 38691 (2016)

[37] Z. Zhu, B. Fauqué, K. Behnia, and Y. Fuseya, J. Phys.: Condens. Matter **30**, 313001 (2018).

[38] Q. H. Yu, Y.-Y. Wang, R. Lou, P.-J. Guo, S. Xu, K. Liu, S. Wang, and T.-L. Xia, Europhys. Lett. **119**, 17002 (2017).

[39] F.-X. Xiang, M. Veldhorst, S.-X. Dou, and X.-L. Wang, Europhys. Lett. **112**, 37009 (2015).